Rare Metal Materials and Engineering
Volume 55, Issue 4, April 2026
Available online at www.rmme.ac.cn

Science Press

Cite this article as: Niu Wenshuai, Li Haiyan, Zeng Linghao, et al. Effects of Crystal Orientations and Grain Boundaries on Nanoindentation Behavior of γ-TiAl Alloys[J]. Rare Metal Materials and Engineering, 2026, 55(04): 899-913. DOI: https://doi.org/10.12442/j.issn.1002-185X.20250129.

ARTICLE

Effects of Crystal Orientations and Grain Boundaries on Nanoindentation Behavior of γ-TiAl Alloys

Niu Wenshuai[1], Li Haiyan[1,2], Zeng Linghao[1], Cao Hui[1,2], Chen Wenke[1,2], Han Chenyang[1], Feng Ruicheng[1,2], Chen Tao[3]

[1] School of Mechanical and Electrical Engineering, Lanzhou University of Technology, Lanzhou 730050, China; [2] Engineering Research Center of Nonferrous Metallurgy's New Equipment, Ministry of Education, Lanzhou University of Technology, Lanzhou 730050, China; [3] School of Mechanical Engineering and Rail Transit, Changzhou University, Changzhou, 213164, China

Abstract: To elucidate the deformation mechanisms of γ-TiAl, the nanoindentation experiments and crystal plasticity finite element (CPFE) simulation were employed to investigate the effects of crystal orientations and GBs on the mechanical properties of γ-TiAl alloys. A crystal plasticity constitutive model was developed, and load-displacement curves, hardness, and Young's modulus were obtained for both single grains and GBs in γ-TiAl alloys. Based on the aforementioned model, this study investigated the distribution patterns of surface morphology around the indentation sites of individual grain and GBs. It also analyzed the cumulative shear strain distribution, slip system activation, and the interaction between GBs and dislocation slip for various crystal orientations. The results indicate that the mechanical response and pileup behavior exhibit significant anisotropy due to the interplay among the indenter geometry, material slip systems, and cumulative shear strain distribution. Moreover, the interaction between GBs and dislocation slip substantially alters dislocation distribution, thereby influencing material flow and playing a critical role in the mechanical response and plastic deformation of the material.

Key words: grain boundary; nanoindentation; anisotropy; crystal orientation; CPFE

1 Introduction

Advanced materials, including high-performance titanium alloys and nickel-based superalloys, have significantly propelled the development of the aerospace industry[1–2]. The application level of titanium-aluminum alloys is closely tied to advancements in aero-engine technology. As a typical high-temperature material, γ-TiAl alloys exhibit exceptional properties, such as low density, high specific strength, high specific stiffness, excellent high-temperature oxidation resistance, and creep resistance. Consequently, these alloys are extensively used in the aerospace and automotive industries and are regarded as one of the most promising high-temperature lightweight structural materials for low-pressure turbine blades[3–5], potentially reducing the mass of an aero-engine by 20%–30%[6]. However, γ-TiAl alloys exhibit poor room-temperature plasticity, with elongation restricted to only 2%–4%, making them susceptible to brittle fracture[7–8]. This characteristic can lead to high manufacturing costs, reduced productivity, and suboptimal machining quality[9–10]. Therefore, the inherent brittleness of γ-TiAl alloys has become a significant bottleneck hindering their broader engineering applications.

To enhance the machinability of γ-TiAl alloys, researchers have explored various aspects of their mechanical properties. Presently, the deformation mechanisms of γ-TiAl alloys are primarily investigated through molecular dynamics (MD) simulations[11–12], mechanical characterization[13], and microstructure observation[14]. The typical microstructure of TiAl alloys is lamellar, consisting of two phases. The γ-phase with an $L1_0$ structure serves as one of its main constituent phases. This microstructure contains numerous complex oriented

Received date: April 12, 2025
Foundation item: National Natural Science Foundation of China (52065036, 52365018); Natural Science Foundation of Gansu (23JRRA760, 24JRRA175, 25JRRA060); Hongliu Outstanding Youth Foundation of Lanzhou University of Technology; Leading Innovative Talents Project of Changzhou (CQ20210111)
Corresponding author: Li Haiyan, Ph. D., Associate Professor, School of Mechanical and Electrical Engineering, Lanzhou University of Technology, Lanzhou 730050, P. R. China, Tel: 0086-931-5135199, E-mail: honey@lut.edu.cn

Copyright © 2026, Northwest Institute for Nonferrous Metal Research. Published by Science Press. All rights reserved.

interfaces that significantly influence its mechanical properties. These interfaces consist of multiple grains and phases separated by GBs (GBs) and phase boundaries[15–16]. Zhang et al[17] used a three-dimensional (3D) phase field simulation method to investigate the nucleation, growth, and coarsening processes of multiple variants in the γ phase of TiAl alloys, elucidating the formation and evolution mechanism of multiphase γ lamellae and revealing the constitutive relationship between morphology and mechanical properties of TiAl alloy. Xiang et al[18] demonstrated that twinning and phase boundaries synergistically improve the strength and ductility of TiAl lamellar single crystals more effectively than phase boundaries alone. Additionally, increasing the twin/phase boundary ratio can significantly enhance the synergistic effect on the strength and plasticity of TiAl single crystals, enhancing their mechanical properties for specific applications. Monchoux et al[19] examined the microstructure, room-temperature tensile properties, and deformation mechanisms of γ-TiAl alloys. The samples were fabricated via spark plasma sintering, and the activated deformation systems were characterized using transmission electron microscope (TEM). TEM analysis revealed that twins are propagated across GBs due to internal stresses induced by the accumulation of Shockley dislocations. Ordinary dislocations, owing to their strong cross-sliding ability, cannot form pileup faults. Zhao et al[20] used MD simulations to investigate the tensile deformation behavior of polycrystalline γ-TiAl with simple and random grain orientations. Their findings indicated severe deformation at GBs, significant GB sliding, and the nucleation and diffusion of dislocations from GBs into the grain interiors. These observations suggest that dislocation motion plays a crucial role in coordinating the mechanical behavior at GBs, while increasing dislocation density near GBs leads to microcrack formation, ultimately contributing to material failure. Zhou et al[21] explored the effect of interfacial spacing λ on the deformation mechanisms of layered γ-TiAl alloys through MD simulations. Results showed that Shockley dislocations tend to nucleate between neighboring interfaces, subsequently moving across the γ/γ interface, leading to interface disruption, crack formation, and structural damage. Cao et al[22] employed MD simulations to investigate the supersonic particle bombardment of a duplex TiAl alloy and analyzed the influence of the γ/α_2 phase interface on the deformation mechanisms and mechanical properties of the TiAl alloy during bombardment. Their findings indicated that the impact deformation mechanisms vary among γ/α_2 models with different thickness ratios, with the deformation predominantly occurring in the γ phase and at the interface. Cao et al[23] investigated the scratch mechanism of polycrystalline γ-TiAl alloy at the atomic scale using MD simulations and analyzed the scratch morphology during the scratching process. Their results indicated that variations in the number of GBs and the randomness of crystal orientation result in diverse stacking patterns on the scratch surface. In summary, current research on the mechanical properties of γ-TiAl alloys primarily relies on atomic-scale theoretical analyses and macroscopic large-deformation tensile tests, which restricts the ability to precisely determine the mechanical properties of individual grain and interface.

Nanoindentation is an effective method for evaluating the mechanical properties of materials at meso- and micro-scales, and has gained popularity for local mechanical characterization of single-crystal and polycrystalline metallic materials due to its high resolution and depth sensing capability during loading[24–26]. However, polycrystalline materials typically contain multiple grains separated by GBs, leading to complex mechanical behavior because of material anisotropy, especially under nanoindentation. The evolution of dislocation structures within grains significantly influences material strengthening and failure mechanisms, which are closely tied to crystal orientation. During nanoindentation, the anisotropy of polycrystalline materials becomes particularly evident, with different grains exhibiting marked variations in mechanical behavior due to their distinct crystal orientations[27]. Filippov et al[28] examined the influence of crystal orientation and indenter direction on indentation hardness and modulus using the Vickers indentation method. Their findings revealed that indentation hardness and modulus exhibit periodic variation with indenter orientation on (100) and (110) oriented surfaces, attributed to the combined effects of indenter geometry and crystal symmetry. Ernst et al[29] examined the influence of crystal orientation on the indentation modulus, hardness, and creep properties of high-purity β-Sn. They demonstrated that the orientation-dependent elastic and plastic deformation behavior is attributed to the anisotropic plastic deformation caused by crystal orientation and the associated slip systems. Tang et al[30] studied the anisotropic hardness, elastic modulus, and dislocation behavior of AlN grains using Berkovich nanoindentation and MD simulations. Their findings revealed a strong correlation between crystal orientation and both hardness and elastic modulus. The relationship between crystal orientation and dislocation slip is determined by analyzing the Schmidt factor for slip system activation in grains with different orientations, as well as by observing pileup and slip lines around the indentations. Li et al[31] derived the deformation mechanisms and accumulation modes from the material pileup distribution observed in nanoindentation experiments, which can elucidate nanoscale mechanical properties, such as strength, ductility, and hardness. Wang et al[32] highlighted that crystal orientation is a critical factor influencing pileup behavior, as different orientations result in distinct pileup distributions. Consequently, the microstructure must be considered when interpreting indentation results.

Nanoindentation involves a complex deformation process, and the analysis of detailed deformation mechanisms within the indentation region is challenging due to the intricate stress conditions that induce heterogeneous strains[33]. In contrast, the crystal plasticity finite element (CPFE) simulation provides a powerful tool for exploring these mechanisms. Through CPFE simulations, it is possible to obtain extensive quantitative information that is difficult to acquire experimentally, such

as geometrically necessary dislocations (GNDs)[34] and shear strains in various slip systems[35]. By integrating CPFE simulations with nanoindentation experiments, significant insights have been gained into plastic anisotropy[36], GB effects[37], and surface morphology[38–39]. Numerous studies have demonstrated the potential of CPFE simulations in capturing crystal anisotropy through investigations on single-crystal and polycrystalline metals[40]. For instance, Wang et al[41] calibrated the constitutive parameters of single-crystal copper by fitting load-displacement curves from CPFE simulations and nanoindentation experiments, revealing that both material orientation and indenter geometry significantly influence surface pileup behavior. They introduced a surface pileup density factor to qualitatively describe this tendency. Han et al[39] examined Ti-6Al-4V nanoindentation using CPFE simulations and experiments, and found that crystal orientation and GBs strongly affect hardness and pileup, highlighting the varying symmetries of nanoindentation relative to the indentation axis at different grain orientations. Wang et al[42] used CPFE simulations and experiments to investigate the nanoindentation behavior of two bi-crystal copper crystals under a Berkovich indenter, revealing that the indentation size effect exhibits crystal orientation-dependent characteristics due to the anisotropy of statistical storage dislocations and GNDs. Additionally, GBs significantly influence the plastic deformation of crystals. Han et al[35] examined the indentation pileup behavior of Ti-6Al-4V alloys through a combination of experiments and CPFE simulations, elucidating the evolution of shear strain in different slip systems and predicting the density distribution of GNDs around indentations. Yin et al[43] employed nanoindentation simulations and experiments to analyze the deformation behavior of the α_2 phase in Ti-43.5Al-4Nb-1Mo-0.1B (at%, TNM) samples, demonstrating that the surface Schmidt factor (SSF) and internal Schmidt factor (ISF) can be used to interpret nanoindentation deformation. Regions with higher SSF are prone to slip and pileup, while a larger ISF can promote slip and reduce shear strain accumulated on surface. Zambaldi et al[44] conducted simulations and experiments on the γ phase in Ti-45.9Al-8Nb, showing that the ease of activation of ordinary dislocation slip at room temperature in γ-TiAl is an intrinsic property, which is not primarily influenced by dislocations originating from or interacting with interfaces. In summary, CPFE simulation offers significant advantages in exploring the detailed deformation mechanisms of nanoindentation. However, further research is needed to refine the complex interactions between various microstructures.

Therefore, this study employed a combination method of CPFE simulations and nanoindentation experiments to investigate the deformation behavior of the γ -phase in TNM alloys and to calibrate the constitutive parameters of γ -TiAl alloys. Additionally, it studied the surface morphology and slip behavior of nanoindentations at both single crystals and GBs to elucidate the microscale differences in plastic deformation among various single crystals. The study also explored how the interaction between indenter geometry and crystal orientation influences surface pileup, as well as the impact of different GBs on plastic deformation. Ultimately, this research established a quantitative correlation between the microscopic deformation mechanisms and macroscopic mechanical behavior of γ-TiAl alloys, providing theoretical support for achieving high-quality surface processing of γ-TiAl alloys and other brittle materials.

2 Experiment

The experimental material used in this study was an extruded bar manufactured by the Institute of Metal Research, Chinese Academy of Sciences, with a nominal chemical composition of Ti-43.5Al-4Nb-1Mo-0.1B (at%, TNM). A bulk sample measuring 16 mm×16 mm×5 mm was extracted from the midsection of the bar via wire electrical discharge machining. The sample surfaces were prepared through a multi-step process. Initially, The sample surfaces were sequentially abraded using progressively finer SiC sandpapers; subsequently, they were polished with colloidal silica suspension containing particles with the diameter of 0.06 μm; finally, electrolytic polishing was performed using a titanium electrolyte solution (comprising 5% perchloric acid, 35% *n*-butanol, and 60% methanol) at −15–0 °C and 25 V for 30 s to prepare the surface for electron backscatter diffractometer (EBSD) analysis.

Nanoindentation experiments were conducted using an Anton Paar MCT-3 nanoindenter in visual matrix mode, enabling multiple consecutive indentations. Samples were selected and indented at both γ-phase single crystals and GBs. A diamond Vickers indenter was employed to penetrate the samples at a constant rate of 2 μm/min until a maximum depth of 500 nm was achieved, followed by retraction to the initial position at the same rate.

Microstructure images of TNM alloys with a spatial resolution of 1 μm were acquired via EBSD. Fig. 1 illustrates the distribution of constituent phases and crystal orientations of TNM alloy. EBSD measurements at seven specific indentation points, as shown in Fig. 1, were conducted to accurately determine the crystal orientation of each grain. Surface morphology surrounding these seven indentation points was characterized using atomic force microscope (AFM, Bruker Dimension Icon) in smart mode. The crystal orientation of grains near these points can be described by distinct Euler angles (φ_1, φ, φ_2). Specifically, the Euler angles for γ-phase single crystals 1, 2, 3, and 4 are (19.1°, 142.6°, 14.8°), (104.9°, 47.2°, 7.8°), (39.6°, 89.2°, 55.1°), and (168.9°, 68.2°, 49.4°), respectively. For GBs, the Euler angles are as follows: for GB 1 between Grain 1 and Grain 2, (19.1°, 142.6°, 14.8°) and (104.9°, 47.2°, 7.8°); for GB 2 between Grains 3 and Grains 4, (39.6°, 89.2°, 55.1°) and (168.9°, 68.2°, 49.4°); for GB 3, (118.1°, 47.4°, 42.0°) and (109.1°, 36.1°, 11.6°). Grains with Euler angles of (39.6°, 89.2°, 55.1°) exhibit the lowest hardness.

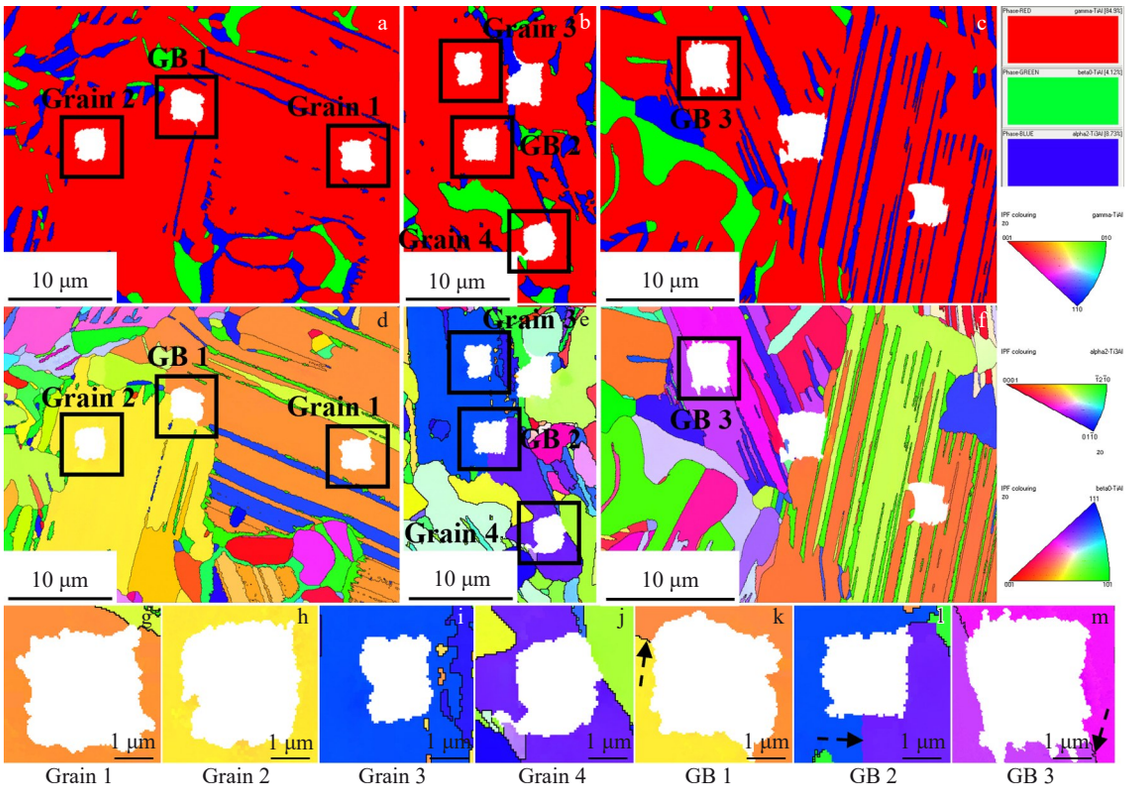

Fig.1 Phase maps (a–c) and inverse polar figures (IPFs) (d–f) of TNM alloy indentation surface; IPFs of seven selected nanoindentation points in Fig.1a–1f (g–m)

3 Crystal Plasticity Theory and Finite Element Modeling

3.1 Crystal plasticity constitutive equation

Based on the works of Asaro et al[45–46], this study developed CPFE framework and methodology. The deformation gradient F can be decomposed into elastic F^{e} and plastic F^{p} components, as illustrated in the following equation:

$$F=F^{\mathrm{e}}F^{\mathrm{p}} \tag{1}$$

where F^{e} represents the elastic stretching and rigid body rotation within the lattice, and F^{p} denotes the plastic deformation gradient.

The velocity gradient L^{p} can be expressed as the sum of the plastic shear strain rate components $\dot{\gamma}^{\alpha}$ in the slip directions of the twelve slip systems of the γ-TiAl alloy, multiplied by the normal vectors of the respective slip planes. This relationship is illustrated in the following equation:

$$L^{\mathrm{p}}=\dot{F}^{\mathrm{p}}(F^{\mathrm{p}})^{-1}=\sum_{\alpha=1}^{12}\dot{\gamma}^{\alpha}\boldsymbol{S}^{\alpha}\times\boldsymbol{m}^{\alpha} \tag{2}$$

where $\boldsymbol{S}^{\alpha}$ represents the slip direction in global coordinates and $\boldsymbol{m}^{\alpha}$ denotes the slip surface normal in global coordinates.

The shear strain rates of the slip system $\dot{\gamma}_{\mathrm{S}}^{\alpha}$ and the twinning system $\dot{\gamma}_{\mathrm{T}}^{\beta}$ can be described by a simple power-law relationship, as shown in the following equations[47]:

$$\begin{cases}\dot{\gamma}_{\mathrm{S}}^{\alpha}=\dot{\gamma}_{0}^{\alpha}\,\mathrm{sgn}\,(\tau_{\mathrm{S}}^{\alpha})\left|\dfrac{\tau_{\mathrm{S}}^{\alpha}}{g_{\mathrm{S}}^{\alpha}}\right|^{m}\\ \dot{\gamma}_{\mathrm{T}}^{\beta}=\dot{\gamma}_{0}^{\beta}\,\mathrm{sgn}\,(\tau_{\mathrm{T}}^{\beta})\left|\dfrac{\tau_{\mathrm{T}}^{\alpha}}{g_{\mathrm{T}}^{\alpha}}\right|^{m}\end{cases} \tag{3}$$

where $\dot{\gamma}_{0}^{\alpha}$ and $\dot{\gamma}_{0}^{\beta}$ are the reference strain rates of the α-slip system and the β-twin system, respectively; $\tau_{\mathrm{S}}^{\alpha}$ and $\tau_{\mathrm{T}}^{\beta}$ are the critical shear stresses of the α-slip system and the β-twin system, respectively; g_{S}^{α} and g_{T}^{α} are the slip deformation resistances or shear resistances of the α-slip system and the β-twin system, respectively; m is the strain rate sensitivity index.

The evolution of yield strength ($\dot{g}^{\alpha}$) during strain strengthening can be described by the following equation[48]:

$$\dot{g}^{\alpha}=\sum_{\beta}h_{\alpha\beta}\dot{\gamma}^{\beta} \tag{4}$$

where $h_{\alpha\beta}$ represents the hardening model, and $\dot{\gamma}^{\beta}$ is the plastic shear strain rate of the β-twin system. The number of twin crystal integrals in the β-twin system (f^{t}) is given by:

$$f^{\mathrm{t}}=\frac{\dot{\gamma}_{\mathrm{T}}^{\beta}}{\gamma_{\mathrm{twin}}} \tag{5}$$

where γ_{twin} represents the twin shear strain (it has a fixed value of 0.707 for γ-TiAl[49]).

In this study, the hardening model proposed by Peirce et al[50] was used. The hardening modulus $h_{\alpha\beta}$ can be determined using the following equation:

$$h_{\alpha\beta}=qh(\gamma) \tag{6}$$

where q is the hardening coefficient. When $\alpha=\beta$, it represents the self-hardening coefficient, that is, the coefficient of hardening effect of the α-slip system on itself, which takes a value of 1. When $\alpha\neq\beta$, q denotes the latent hardening coefficient, that is, the coefficient of hardening effect of the α-slip system on other slip systems, which takes a value of 1.4. $h(\gamma)$ is a function of γ, as shown in the following equation:

$$h(\gamma) = h_0 \operatorname{sech}^2\left|\frac{h_0\gamma}{\tau_s - \tau_0}\right| \tag{7}$$

where h_0, τ_0, and τ_s represent the initial hardening modulus, the initial critical shear stress, and the breakthrough stress at the onset of the macroplastic flow, respectively. γ denotes the Taylor cumulative shear strain over all active slip systems, as presented in the following equation:

$$\gamma = \sum_{\alpha}\int_0^t \left|\dot{\gamma}^{\alpha}\right| \mathrm{d}t \tag{8}$$

3.2 Finite element modeling

The crystal plasticity constitutive model was implemented into the explicit finite element code Abaqus/Explicit through the VUMAT user subroutine to develop a 3D CPFE model for nanoindentation testing. Fig.2a illustrates the 3D CPFE model for the γ-TiAl single crystal nanoindentation test, containing a square TiAl sample and a rigid diamond indenter. The square sample measures 15 μm×15 μm×7 μm and is discretized into 63 840 reduced-integration eight-node linear hexahedral elements (C3D8R). The rigid Vickers indenter is meshed with 1872 C3D8R. The indentation simulation employs depth control with a loading rate of 33.33 nm/s, a maximum indentation depth of 500 nm, and an unloading rate of 33.33 nm/s. To enhance computational efficiency, a transition mesh refines the contact region between the indenter and the sample. The bottom surface of the sample is fully constrained, and the contact interface between the indenter and the sample is assumed to be frictionless.

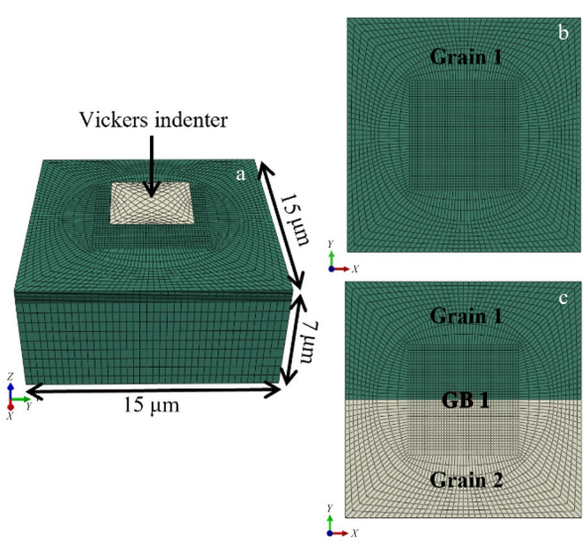

Fig.2 Schematic diagrams of 3D CPFE model with nanoindentation: (a) single crystal square sample and standard Vickers indenter; (b) top view of single crystal square sample; (c) top view of bi-crystal square sample

To investigate the influence of GBs on nanoindentation results, a bi-crystal nanoindentation 3D CPFE model was developed, as illustrated in Fig. 2c. This model contains a square TiAl alloy sample and a rigid diamond Vickers indenter. The substrate consists of two grains with distinct crystallographic orientations (as shown in Fig. 1k–1m), where different colors indicate different crystallographic orientations. The dimensions of the square sample are 15 μm× 15 μm×7 μm, and the meshing type, constraints, contact settings, and loading/unloading settings are consistent with those used for the single-crystal sample.

4 Results and Discussion

4.1 Calibration of constitutive parameters

In this study, nanoindentation mechanical response analysis was employed to determine the constitutive parameters of γ-TiAl in the TNM alloy. The constitutive parameters encompass the reference strain rate, strain rate sensitivity index, initial hardening modulus, initial critical shear stress, and breakthrough stress at large plastic deformation. Based on previous studies[44,51], the initial parameters were set as follows: the reference strain rate for the ordinary slip system, super slip system, and twinning system was 0.001 s^{-1}; the strain rate sensitivity index was 20; the initial hardening modulus was 300 MPa; for ordinary slip system, super slip system, and twinning system, the initial critical shear stresses were 55, 165, and 110 MPa, and the breakthrough stresses were 400, 1200, and 800 MPa, respectively. Nanoindentation experiments were conducted on different grains, and CPFE simulations were used to model the mechanical response. CPFE simulation results were then fitted to the experimental nanoindentation data to calibrate the constitutive parameters of γ-TiAl in TNM alloy. Additionally, γ-TiAl has six independent elastic constants: C_{11}, C_{12}, C_{13}, C_{33}, C_{44}, and C_{66}, which are presented in Table 1.

The γ-TiAl alloy exhibits an $L1_0$ lattice structure. Its plastic deformation mechanisms include four ordinary slip systems of $\{111\}\langle 1\bar{1}0\rangle$, eight super slip systems of $\{111\}\langle 10\bar{1}\rangle$, and four twinning systems of $\{111\}\langle 11\bar{2}\rangle$. The specific details of these slip and twinning systems are summarized in Table 2, while the calibrated constitutive parameters for γ-TiAl are presented in Table 3. The calibrated critical resolved shear stress (CRSS) values for ordinary slip systems, twinning systems, and super slip systems are 400, 500, and 600 MPa, respectively.

Fig. 3a–3d illustrate the load-displacement curves for four distinct crystal orientations derived from CPFE simulations and nanoindentation experiments. The crystal orientation data were obtained from EBSD results presented in Fig. 1g–1j, which show that there is a strong correlation between the simulated and experimental curves.

The indentation experiments and simulations reveal distinct

Table 1 Elastic constants of γ-TiAl in TNM alloy (GPa)

C_{11}	C_{12}	C_{13}	C_{33}	C_{44}	C_{66}
190	105	90	185	120	50

Table 2 Slip and twinning systems for γ-TiAl[52]

System	Mechanism	Classification	Index
(111)[1$\bar{1}$0]	Ordinary	Transversal	1
(111)[01$\bar{1}$]	Super	Transversal	2
(111)[10$\bar{1}$]	Super	Mixed	3
($\bar{1}$11)[110]	Ordinary	Mixed	4
($\bar{1}$11)[01$\bar{1}$]	Super	Transversal	5
($\bar{1}$11)[101]	Super	Transversal	6
(1$\bar{1}$1)[110]	Ordinary	Longitudinal	7
(1$\bar{1}$1)[011]	Super	Transversal	8
(1$\bar{1}$1)[10$\bar{1}$]	Super	Longitudinal	9
(11$\bar{1}$)[1$\bar{1}$0]	Ordinary	Mixed	10
(11$\bar{1}$)[011]	Super	Transversal	11
(11$\bar{1}$)[101]	Super	Transversal	12
(111)[11$\bar{2}$]	Twining	Transversal	13
($\bar{1}$11)[$\bar{1}$1$\bar{2}$]	Twining	Transversal	14
(1$\bar{1}$1)[1$\bar{1}\bar{2}$]	Twining	Longitudinal	15
(11$\bar{1}$)[112]	Twining	Transversal	16

Table 3 Calibrated γ-TiAl constitutive parameters for γ-TiAl

Mechanism	$\lvert\dot{\gamma}_0\rvert$	m	h_0/MPa	τ_s/MPa	τ_0/MPa
Ordinary	0.001	20	400	440	400
Super	0.001	20	500	660	600
Twin	0.001	20	400	550	500

differences in the mechanical properties of γ -TiAl with varying crystal orientations. The hardness values for each grain were derived from the unloading segment of the load-displacement curves in Fig. 3, using the standard Oliver-Pharr indentation test method[53]. Table 4 and Table 5 present the experimental and simulated hardness and Young's modulus for each grain. The experimental hardness of the material, across different crystal orientations, varies from 4.760 GPa to 5.117 GPa, demonstrating a clear orientation dependence. This variation is attributed to the slip systems activated by different crystal orientations. The maximum discrepancy between experimental and simulated hardness and Young's modulus is less than 5%, validating the accuracy of the calibrated constitutive parameters through the consistency of the load-displacement curves, hardness, and Young's modulus data.

4.2 Effect of crystal orientation on plastic deformation

Fig. 4 illustrates the surface morphology and corresponding AFM images of the four selected grain nanoindentation simulations. It is evident that pileups consistently form around the perimeters of the indentations. However, significant variations are observed in the precise location, height, and shape of these pileups across different crystal orientations. Specifically, Grain 1 and Grain 4 exhibit similar two-fold symmetric pileup topographies on either side of the indentations, while Grain 2 displays three-fold symmetry, and Grain 3 shows four-fold symmetry. The surface morphology observed in the experimental AFM images closely resembles that observed in CPFE simulation results, thereby validating the reliability of the simulations. Notably, the depth in AFM images appears shallower compared to the simulation outcome. This discrepancy can be attributed to restrictions in the vibration frequency and tip size of AFM probe, which

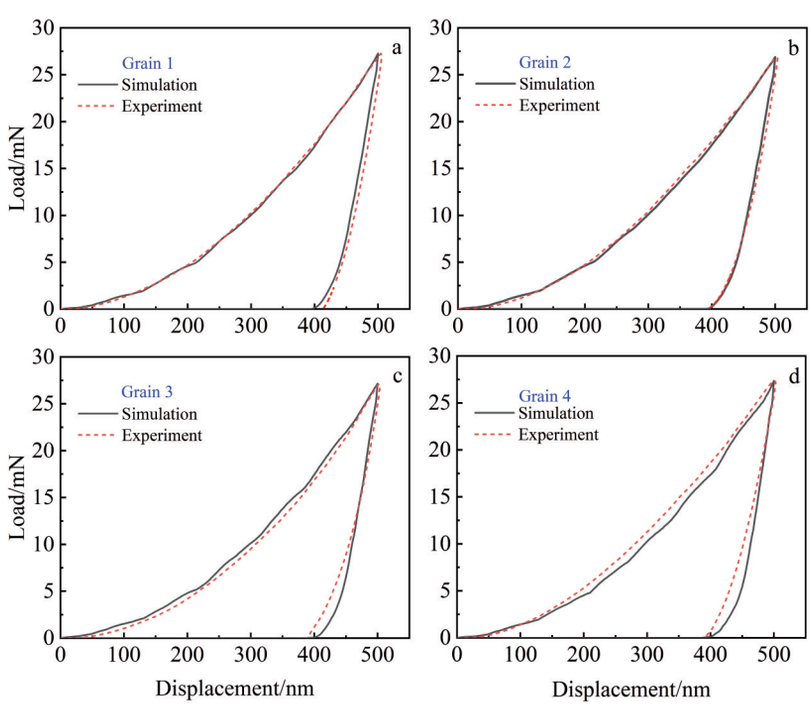

Fig.3 Load-displacement curves for different crystal orientations derived from CPFE simulations and nanoindentation experiments: (a) Grain 1; (b) Grain 2; (c) Grain 3; (d) Grain 4

Table 4 Hardness of each grain obtained by nanoindentation experiments and CPFE simulations

Grain	Euler angle/(°)	Hardness/GPa	
		Experiment	Simulation
1	(19.1, 142.6, 14.8)	4.806	4.875
2	(104.9, 47.2, 7.8)	4.768	4.802
3	(39.6, 89.2, 55.1)	4.760	4.856
4	(168.9, 68.2, 49.4)	5.117	4.894

Table 5 Young's modulus of each grain obtained by nanoindentation experiments and CPFE simulations

Grain	Euler angle/(°)	Young's modulus/GPa	
		Experiment	Simulation
1	(19.1, 142.6, 14.8)	178.56	182.43
2	(104.9, 47.2, 7.8)	171.66	173.15
3	(39.6, 89.2, 55.1)	171.46	170.68
4	(168.9, 68.2, 49.4)	153.25	156.57

prevent full scanning of the indentation bottom region, particularly when the scan area is convex and the indentation pit is small.

The simulated pileup height curves for different crystal orientations in the AB and CD sections are illustrated in Fig.5. In conjunction with the findings presented in Fig. 4, it is evident that the maximum pileup heights vary significantly among different crystal orientations, ranging from 45 nm to 80 nm. The experimentally measured pileup heights exceed the simulated values, potentially due to thermal carbon accumulation resulting from electron beam bombardment during SEM and EBSD observations. Additionally, although electropolishing reduces the surface roughness of experimental samples, residual peaks and valleys remain, whereas the surfaces of simulated samples are perfectly smooth. This discrepancy in surface conditions further contributes to the differences observed between experimental and simulated pileup heights. Overall, the pileup morphology of γ-TiAl alloy under nanoindentation exhibits a pronounced orientation dependence, which is closely associated with slip behavior around the indented region.

During nanoindentation loading, the material at the indenter tip flows towards the surface, accompanied by elastic-plastic deformation. Upon unloading, the elastic component of this deformation gradually recovers. The pileup on the material surface is closely associated with plastic deformation resulting from dislocation slip. To understand the cause of plastic deformation anisotropy, the simulated local deformation field was analyzed. Fig.6a–6d illustrate the total accumulated shear strain (stored in VUMAT state variable) at the maximum indentation depth for all active slip systems obtained from CPFE simulations of four grains. The shear strain peaks at the deepest point of indentation and diminishes toward the outer regions. This finding aligns with classical theories of plastic deformation under indentation[54], which posits that maximum stress concentration occurs at the indentation center. The stress distribution is significantly influenced by the crystal orientation of individual grain, leading to varying maximum values of the total cumulative shear strain among the four grains. This indicates that dislocation slip behavior differs markedly between grains, and grain anisotropy plays a critical role in determining the stress distribution and deformation behavior under indentation.

To gain a deeper understanding of slip behavior across various regions, Fig. 7 illustrates the cumulative shear strains in different grains within both slip systems and twinning systems (including ordinary slip and twinning) from the simulation. The critical shear strain for the γ-TiAl super slip system is notably high, making it difficult to activate; consequently, its cumulative shear strain is minimal. Due to the selective activation of different slip systems, individual grain exhibits significant variations in plastic deformation under indentation. Specifically, Grains 1–3 experience severe plastic deformation in ordinary slip systems, while Grain 4 shows pronounced deformation in twinning systems. These differences are primarily attributed to the crystal orientation and the direction of the applied load. In conjunction with

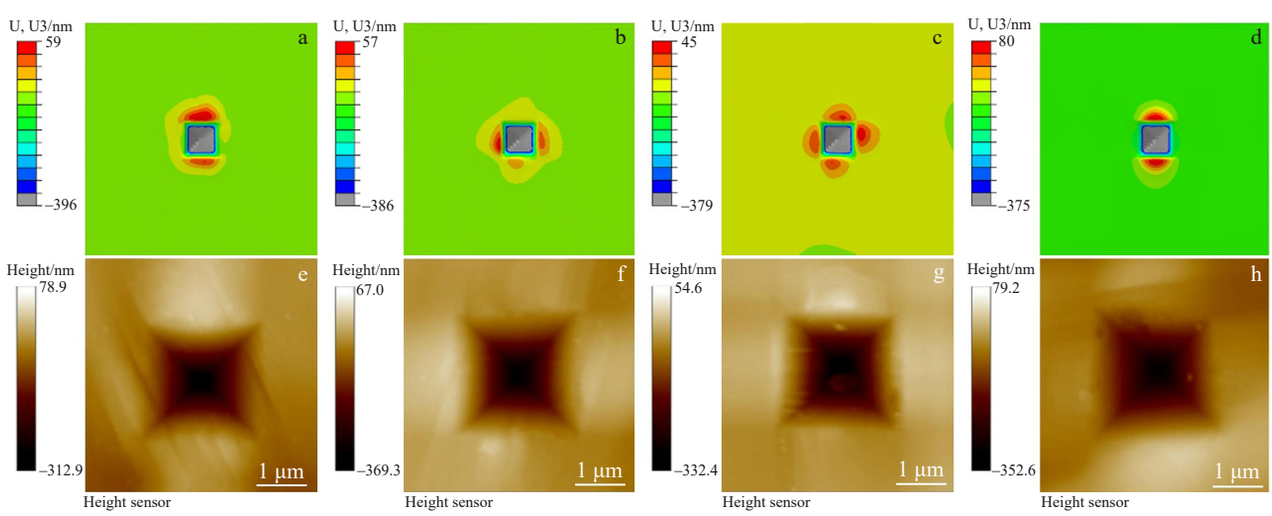

Fig.4 Simulated surface morphologies (a–d) and corresponding AFM images (e–h) of Grain 1 (a), Grain 2 (b), Grain 3 (c), and Grain 4 (d)

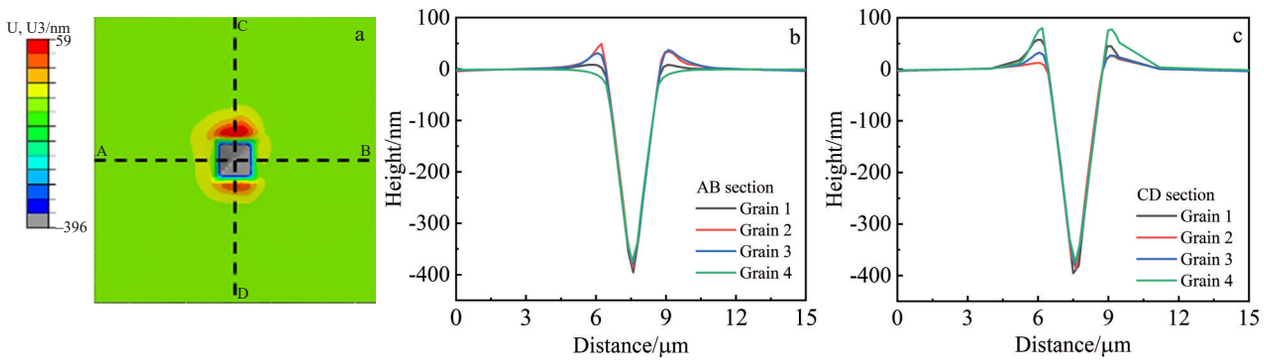

Fig.5 Top view of simulated single crystal model (a); simulated vertical distance profiles of different grains in AB (b) and CD (c) sections in Fig.5a

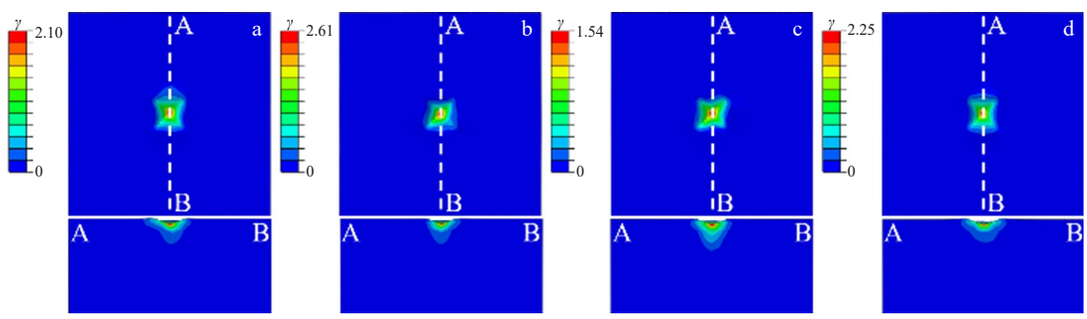

Fig.6 Total cumulative shear strain γ at the maximum indentation depth of different grains: (a) Grain 1; (b) Grain 2; (c) Grain 3; (d) Grain 4

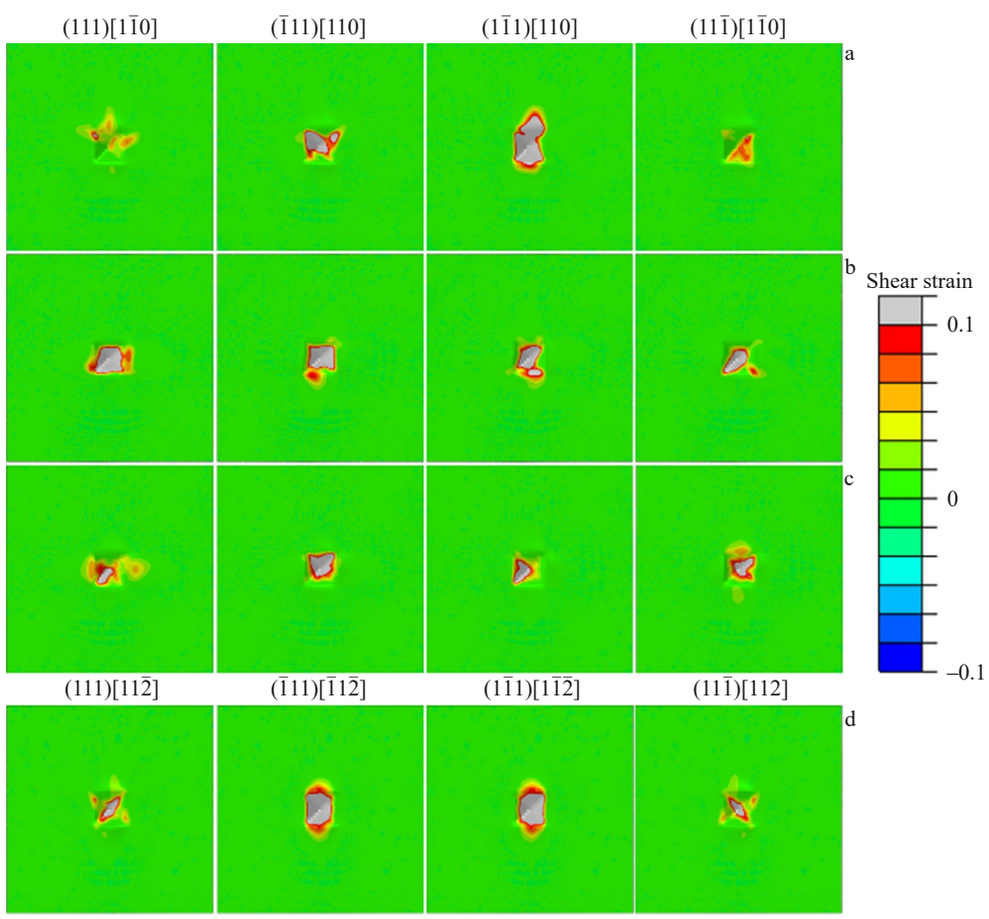

Fig.7 Simulation of cumulative shear strains of different grains within slip systems and twinning systems: (a) Grain 1; (b) Grain 2; (c) Grain 3; (d) Grain 4

Fig.4, it is evident that material pileup is more pronounced in regions experiencing severe plastic deformation. As illustrated in the slip systems presented in Table 2, the double pileup of Grain 1 is dominated by two groups of ordinary slip systems: (111) [1$\bar{1}$0] and (1$\bar{1}$1) [110]. The triple pileup of Grain 2 is dominated by three groups of ordinary slip systems: (111)[1$\bar{1}$0] , ($\bar{1}$11)[110], and (1$\bar{1}$1)[110]. The quadruple pileup of Grain 3 is dominated by four groups of ordinary slip systems: (111)[1$\bar{1}$0], ($\bar{1}$11)[110], (1$\bar{1}$1)[110], and (11$\bar{1}$)[1$\bar{1}$0]. And the double pileup of Grain 4 is dominated by two groups of twinning systems: ($\bar{1}$11)[$\bar{1}$1$\bar{2}$] and (1$\bar{1}$1)[1$\bar{1}$$\bar{2}$].

To investigate the effect of crystal anisotropy on slip system activation, Fig. 8 presents top views of the spatial structure of slip systems in different grains with varying crystal orientations under nanoindentation. Each figure includes a stereo view of the crystal orientation from EBSD data in the lower right corner. The results demonstrate that slip system activation is strongly influenced by crystal orientation, resulting in significant differences in plastic deformation and surface pileup morphology. This finding underscores the importance of the interaction between crystal orientation and slip behavior during nanoindentation, highlighting the complexity of the underlying mechanisms. The observed asymmetry in pileup distribution can be attributed to the interplay between the symmetry of crystal slip system and the geometry of indenter. Moreover, the specific geometry of indenter may favor plastic slip in certain directions. For instance, when the indenter is loaded in the direction indicated by the blue arrow, it activates the slip system shown by the red arrow, leading to material pileup along the indenter boundary, as illustrated in Fig. 4. This phenomenon elucidates the intricate relationship between crystal slip system symmetry and indenter geometry, suggesting a potential mechanism for controlling plastic deformation during nanoindentation.

The complex interaction between the symmetry of crystal slip system and the indenter geometry significantly influences the plastic deformation behavior of materials. Therefore, it is crucial to examine how indenter geometry affects

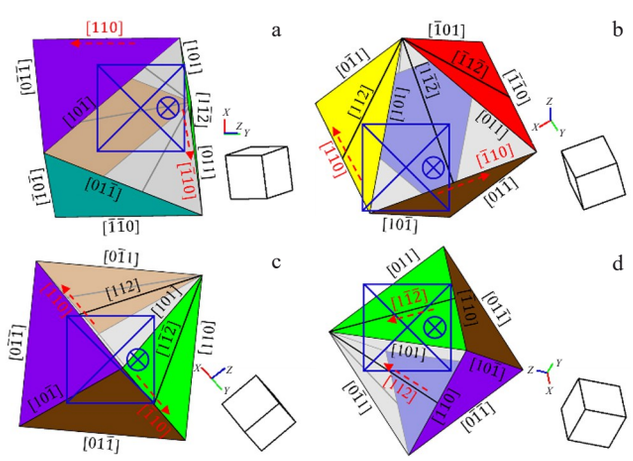

Fig.8 Top views of spatial structure of slip systems in different grains with varying crystal orientations under nanoindentation: (a) Grain 1; (b) Grain 2; (c) Grain 3; (d) Grain 4

nanoindentation behavior. The symmetry of the Vickers indenter around the indentation axis is different from the isotropy of conical and spherical indenters. Consequently, the orientation of the Vickers indenter can influence nanoindentation results. In addition to the indenter orientation illustrated in Fig. 2, this study also simulated and investigated, under other two distinct crystal orientations, as shown in Fig. 9b and 9d. Specifically, the crystal orientation for Fig. 9a–9b corresponds to that depicted in Fig. 1g, while the orientation for Fig. 9c–9d matches that of Fig. 1f. Observations reveal that at identical crystal orientations, different indenter orientations yield varying pileup morphologies, indicating a significant effect of indenter orientation on nanoindentation outcomes. Despite differences in indenter orientation, the pileup positions remain largely consistent, suggesting that material flow during nanoindentation tends to follow specific directions in crystalline materials.

To illustrate this phenomenon, Fig. 10 presents the cumulative shear strains of two grains in different slip and twinning systems under varying indenter orientations. Grain 1 is shown in Fig. 10a and 10b, while Grain 2 is depicted in Fig. 10c and 10d. It can be observed that the cumulative shear strain distributions in the slip systems are consistent between Fig. 10a and 10b, as well as between Fig. 10c and 10d. Severe plastic deformation occurs in the ordinary slip systems, indicating that the activation of slip systems remains unchanged regardless of indenter orientation. This consistency persists despite different crystal orientations of the two grains, suggesting that crystalline materials tend to deform along specific directions during nanoindentation.

Fig. 11 illustrates the load-displacement curves of two grains under varying indenter orientations, revealing distinct differences. Specifically, Grain 2 exhibits minimal variation in its load-displacement curves with a maximum load difference of 0.22, whereas Grain 1 shows significant differences with a maximum load difference of 0.66. This observation suggests that the sensitivity of nanoindentation to indenter orientation

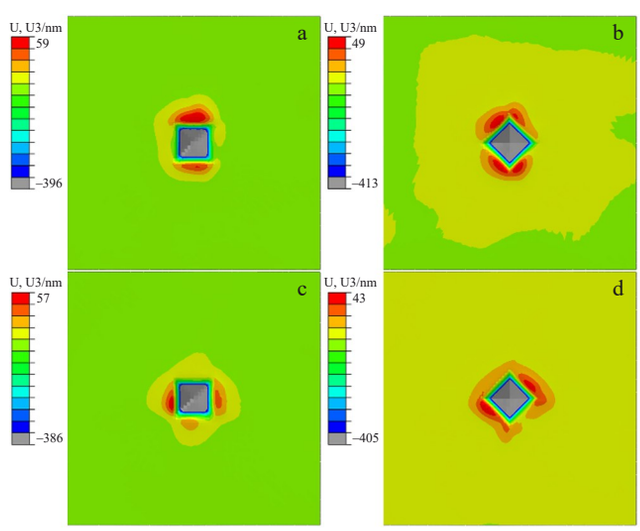

Fig.9 Simulation of surface morphologies under different indenter orientations: (a–b) Grain 1; (c–d) Grain 2

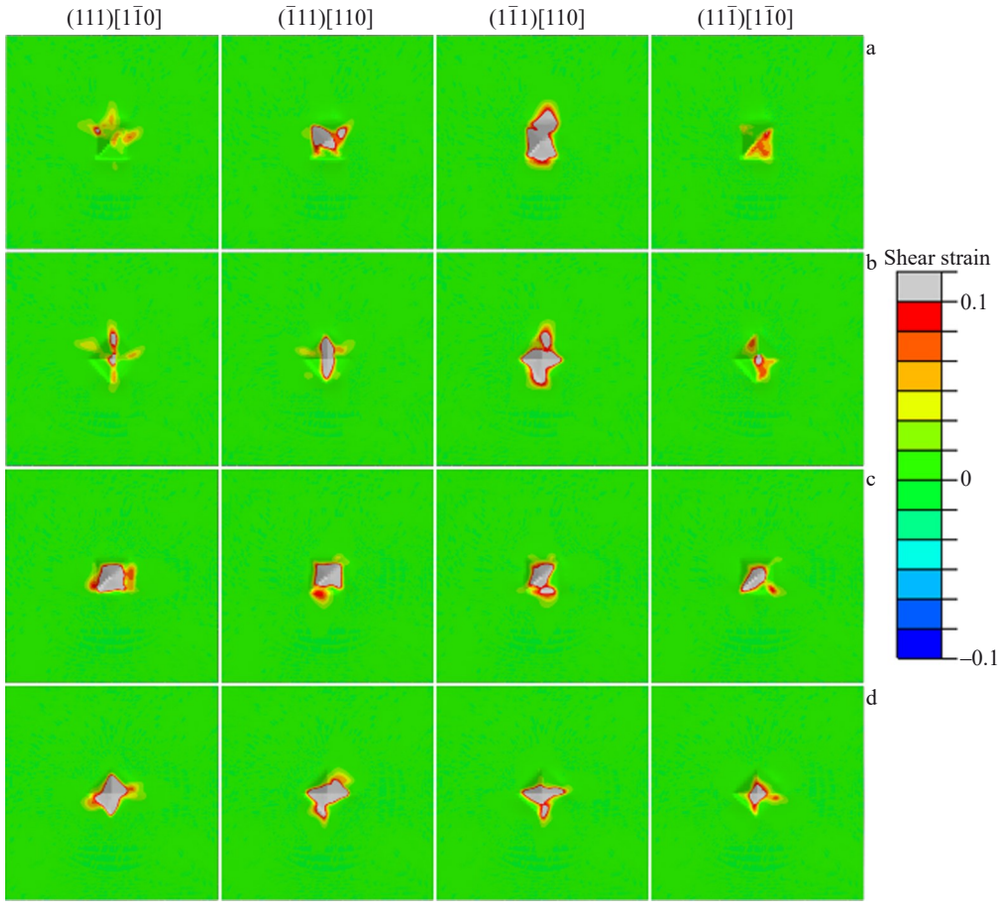

Fig.10 Cumulative shear strain of Grain 1 (a–b) and Grain 2 (c–d) in different slip and twinning systems under different indenter orientations

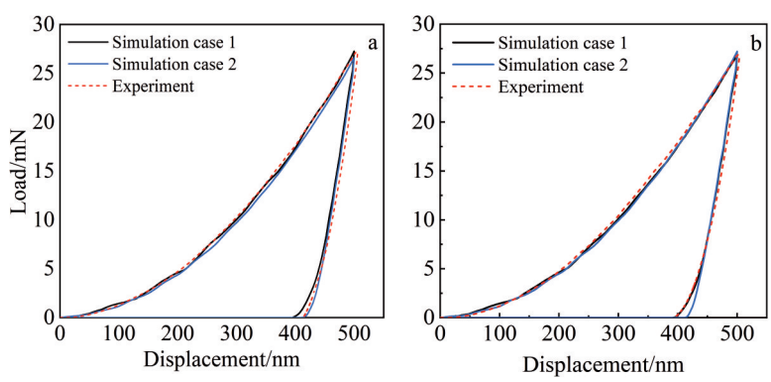

Fig.11 Load-displacement curves of different grains under different indenter orientations: (a) Grain 1; (b) Grain 2

varies with crystal orientation, attributable to different symmetries of crystal orientations relative to the indentation axis. This phenomenon underscores the intricate interaction between the symmetry of crystal slip system and the geometry of the indenter.

4.3 Effect of GBs on mechanical properties

When plastic deformation during indentation interacts with GBs, these boundaries significantly influence outcomes such as hardness and dislocation motion[55]. To investigate the impact of GBs on nanoindentation results, a bi-crystal nanoindentation model was developed, as illustrated in Fig.2c, where two distinct crystal orientations were assigned to the bi-crystal structure. Fig.12 presents the load-displacement curves for the three GBs obtained from both CPFE simulations and nanoindentation experiments, using orientation data provided by EBSD (Fig. 1k – 1m). The results indicate that CPFE simulation used in this study accurately predicts the load-displacement curves of nanoindentation at GBs. Table 6 compares the experimental and simulated values of hardness and Young's modulus at the three GBs, showing a maximum error within 5%, which further validates the accuracy of the calibrated model parameters.

Fig. 13 illustrates the surface morphologies and corresponding AFM images of nanoindentation simulations at three GBs.

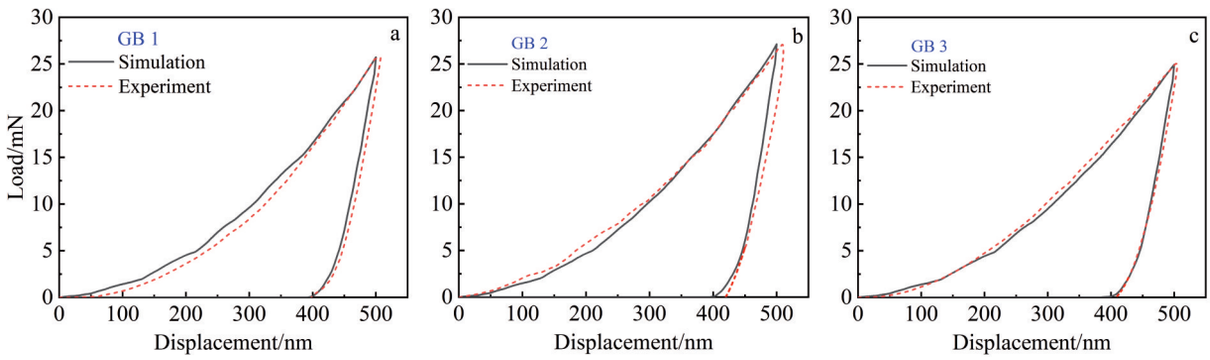

Fig.12 Load-displacement curves at different GBs: (a) GB 1; (b) GB 2; (c) GB 3

Table 6 Hardness and Young's modulus of each GB obtained by nanoindentation experiments and CPFE simulations

GB	Hardness/GPa		Young's modulus/GPa	
	Experimental	Simulated	Experiment	Simulation
1	4.600	4.583	160.56	166.49
2	4.756	4.848	170.56	175.88
3	4.518	4.431	159.78	163.58

In conjunction with Fig. 4, it is evident that GBs induce significant variations in pileup behavior. The pileup distribution characteristics of grains adjacent to the GBs closely resemble those observed in single crystals, yet distinct changes occur specifically within the GB regions. The surface morphologies depicted in the experimental AFM images aligns well with CPFE simulation results, thereby validating the reliability of these simulations. Moreover, the pileup distributions around indentations at the three GBs exhibit notable differences: GB 1 and GB 2 exhibit quadruple pileup, whereas GB 3 exhibits triple pileup. Although the pileup distributions of GB 1, GB 2, and GB 3 are all bisected by the GBs, there are substantial differences in the height and the respective distribution areas. Fig.14 further presents the pileup height curves for nanoindentation AB and CD sections at different GBs obtained from CPFE simulations. Combined with Fig.5, it is clear that the maximum pileup heights on both side of each GB are lower than those observed in single grains. These findings underscore the significant influence of GBs on the plastic deformation during nanoindentation of the material.

Fig. 15 illustrates the comparison of total cumulative shear strain at the maximum indentation depth for single grain and GBs. Specifically, Fig. 15a and 15b depict Grain 1 and Grain 2, while Fig. 15c focuses on GB 1. Similarly, Fig. 15d and 15e present Grain 3 and Grain 4, with Fig. 15f highlighting their GB. The interaction between crystal orientation and GB significantly alters the distribution of plastic deformation under indentation. Different crystal orientations activate distinct slip systems, leading to varied dislocation slips that couple with GB, thereby influencing stress distribution and deformation behavior during indentation. In conjunction with Fig. 4 and Fig. 13, it is evident that the GBs exhibit characteristics similar to single grains, with more pronounced pileup in regions with high cumulative shear strain. Moreover,

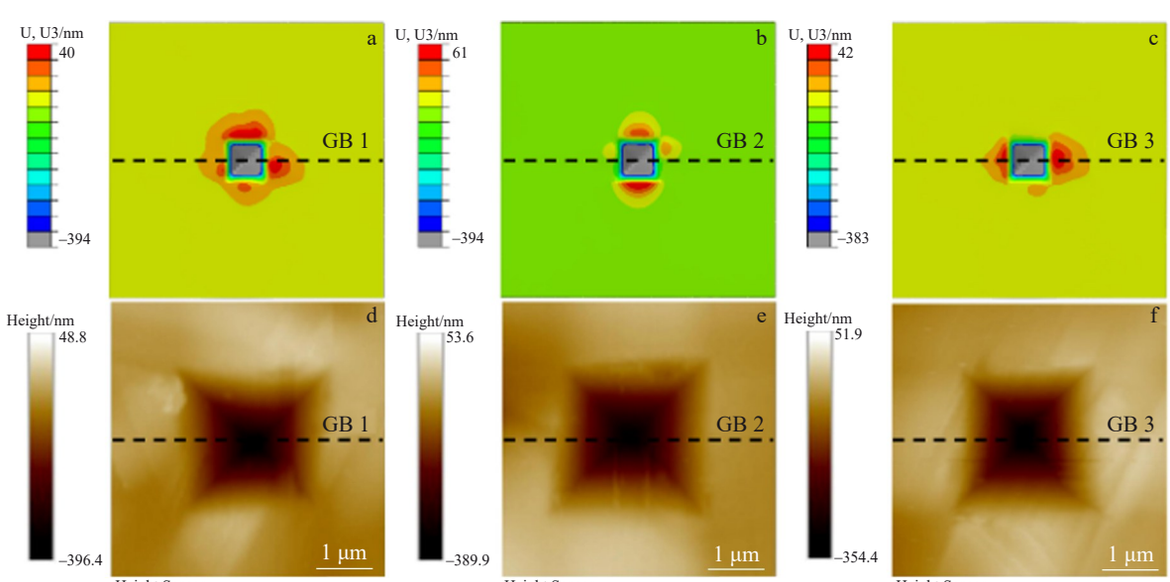

Fig.13 Simulated surface morphologies and corresponding AFM images of each GB in Fig.1: (a) GB 1; (b) GB 2; (c) GB 3

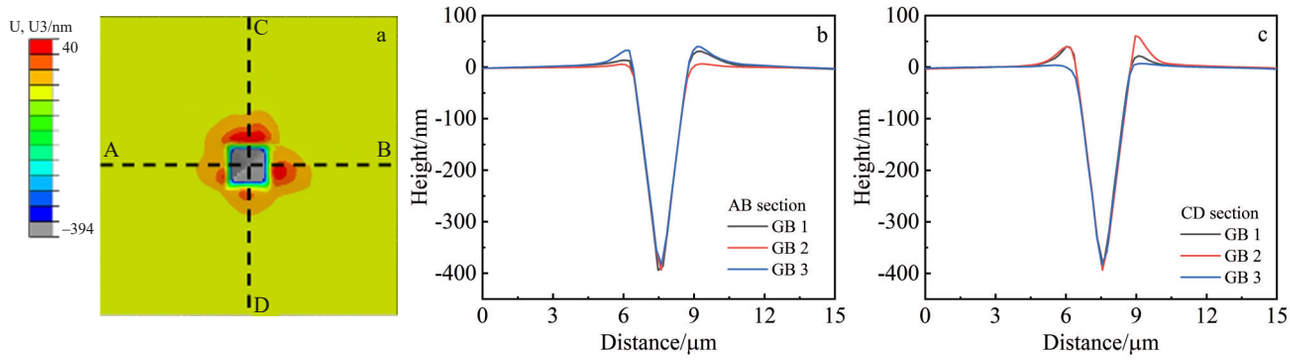

Fig.14 Top view of simulated bi-crystal model (a); simulated vertical distance profiles of different GBs in AB (b) and CD (c) sections

the GB absorbs the accumulated shear strain from the indented area, resulting in lower cumulative shear strain on both side of GB compared to single grain, thus reducing the pileup on both sides.

GB interacts with dislocation slip of varying crystal orientations, significantly altering the distribution of plastic deformation. The interaction between dislocations and GBs exerts a profound influence on plastic deformation. Depending on the crystal orientation of neighboring grains, the nature of GB, and the characteristics of dislocations, multiple dislocation-GB interactions can occur simultaneously. Specifically, near the GB, the variation in indentation response is strongly influenced by the competition between strengthening and softening mechanisms, leading to GB-dependent indentation resistance[56–58]. Strengthening mechanisms involve the accumulation of dislocations at GBs, while softening mechanisms encompass dislocation absorption, slip along GBs, reemission from GBs, and transfer through GBs. The misorientation angle in TiAl alloys is predominantly characterized by high-angle GBs (HAGBs, >15°), with a relatively rare occurrence of low-angle GBs (⩽15°). For GB 1 and GB 2 presented in this study, the misorientation angles are 122° and 129° , respectively, classifying them as HAGBs. HAGBs enhance material toughness and fatigue resistance but may reduce material strength if present in excess. This affects the balance between strengthening and softening mechanisms, significantly impacting mechanical properties. Dislocation-GB interactions, wherein dislocation absorption at GBs becomes predominant, result in a softening mechanism that significantly reduces hardness, as evidenced by the data in Table 4 and Table 6.

To further investigate the influence of GBs on nanoindentation, a bi-crystal nanoindentation model with two distinct crystal orientations was employed (Grain 1 and Grain 2, as shown in Fig.1). The indenter tip was positioned on the side of Grain 2. The simulations for various distances between the indenter tip and the GB were conducted, specifically at 600, 900, 1200, 1500, 1800, 2100, 2400, 2700, and 3000 nm. As illustrated in Fig.16, the load-displacement curves exhibit the greatest deviation from single-crystal simulation curves

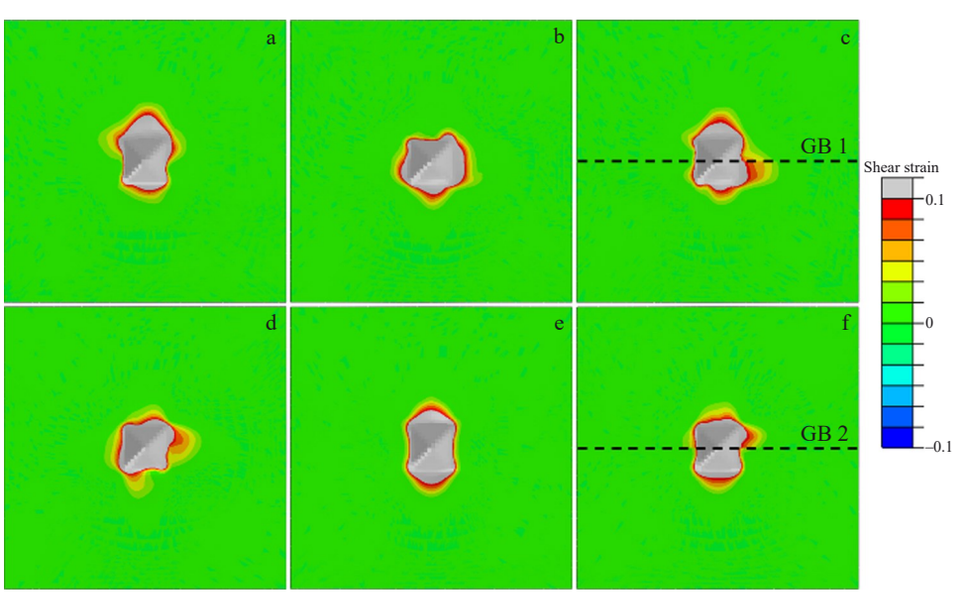

Fig.15 Total cumulative shear strain at maximum indentation depth for different single grains and GBs: (a) Grain 1; (b) Grain 2; (c) GB 1; (d) Grain 3; (e) Grain 4; (f) GB 2

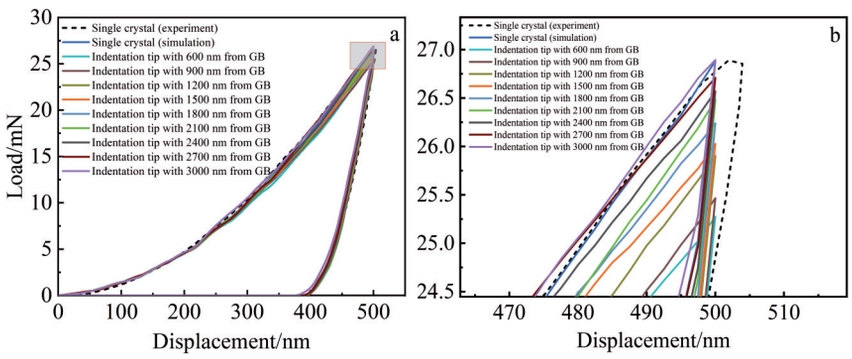

Fig.16 Load-displacement curves (a) and its partial magnification curves (b) of indentation tip located at different distances from GB

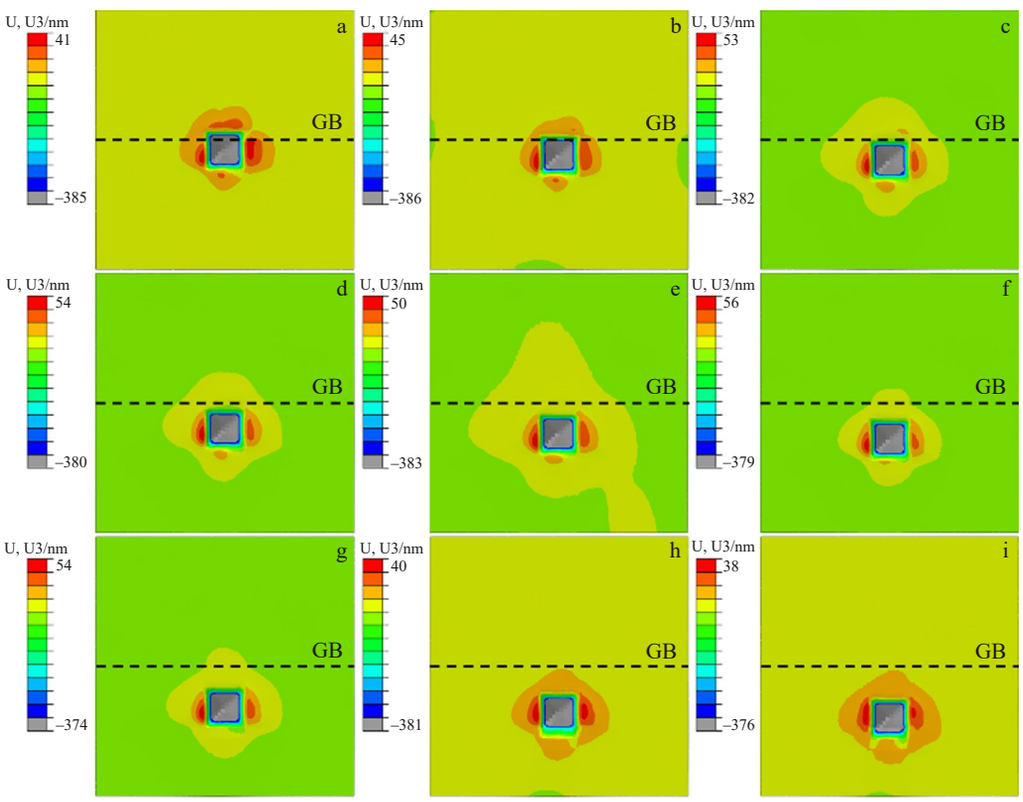

Fig.17 Simulated pileup patterns on indented surfaces with indenter tip located at different distances from GB: (a) 600 nm, (b) 900 nm, (c) 1200 nm, (d) 1500 nm, (e) 1800 nm, (f) 2100 nm, (g) 2400 nm, (h) 2700 nm, and (i) 3000 nm

when the indenter tip is 600 nm away from GB. Conversely, when the indenter tip is 3000 nm away from GB, the load-displacement curve of bi-crystal simulation closely resembles that of a single-crystal simulation. Fig.17 illustrates the pileup patterns on the indentation surface at different distances from the indenter tip to the GB. Due to the presence of GBs, these pileup patterns differ significantly from those observed in single crystals (as shown in Fig.4). Notably, the differences in pileup morphology are most pronounced when the indenter tip is closer to GB, which underscores the significant impact of GBs on nanoindentation behavior.

In summary, the interaction between crystal orientation and GBs significantly influences the mechanical properties of the material. GBs absorb a portion of dislocations and alter the distribution characteristics of plastic deformation under indentation, leading to notable differences in material pileup and a reduction in hardness. When the indentation is sufficiently distant from the GBs, their influence on nanoindentation diminishes.

5 Conclusions

1) The crystal plasticity constitutive parameters of γ-TiAl alloys were calibrated by fitting the simulated and experimental mechanical responses. The calibrated CRSS values for ordinary slip systems, twinning systems, and super slip systems are 400, 500, and 600 MPa, respectively. According to the developed crystal plasticity constitutive model, the simulated load-displacement curves, hardness, and

Young's modulus at single grains and GBs exhibit excellent agreement with the experimental results, thereby validating the accuracy of the calibrated parameters.

2) The hardness of γ-TiAl varies between 4.760 GPa and 5.117 GPa across different crystal orientations, demonstrating a significant dependence on crystal orientation. Specifically, grains with Euler angles of (39.6°, 89.2°, 55.1°) exhibit the lowest hardness. During nanoindentation, crystal orientation influences the activation of slip systems in γ-TiAl. The coupling effect of the symmetry of slip system and the indenter geometry affects plastic deformation and indentation surface morphology, leading to slip and pileup in regions with high cumulative shear strain on the surface. CPFE simulation results align well with the pileup patterns observed in AFM images, validating the reliability of the simulation.

3) The symmetry of Vickers indenter around the indentation axis is different from the isotropy of conical and spherical indenters, and its orientation significantly influences nanoindentation results. Even under identical crystal orientations, varying indenter orientations lead to distinct pileup morphologies, demonstrating that indenter orientation affects nanoindentation outcomes. Despite differences in indenter orientation, the pileup locations remain largely consistent, suggesting that material flow during nanoindentation of crystalline materials tends to follow a specific direction. The varying sensitivity of nanoindentation results to indenter orientation across different crystal orientations can be attributed to different symmetries relative to the indentation axis.

4) The interaction between GBs and crystal orientation significantly influences nanoindentation results. As the indentation tip approaches closer to the GBs, this influence intensifies. During nanoindentation, GBs absorb dislocations and alter the distribution of plastic deformation beneath the indenter. Consequently, this leads to a reduction in hardness, changes in material pileup morphology, and diminishes pileup.

References

1 Ulutan D, Ozel T. *International Journal of Machine Tools and Manufacture*[J], 2011, 51(3): 250

2 Boyer R, Briggs R. *Journal of Materials Engineering and Performance*[J], 2005, 14: 681

3 Bauer V, Christ H J. *Intermetallics*[J], 2009, 17(5): 370

4 Clemens H, Mayer S. *Materials at High Temperatures*[J], 2016, 33(4–5): 560

5 Perrut M, Caron P, Thomas M *et al. Comptes Rendus Physique*[J], 2018, 19(8): 657

6 Kothari K, Radhakrishnan R, Wereley N M. *Progress in Aerospace Sciences*[J], 2012, 55: 1

7 Xia Z W, Shan C W, Zhang M H *et al. Chinese Journal of Aeronautics*[J], 2023, 36(7): 40

8 Appel F, Paul J D H, Oehring M. *The Deutsche Nationalbibliothek*[M]. Leipzig: Deutsche Nationalbibliografie, 2011: 69469

9 Aspinwall D, Dewes R, Mantle A. *CIRP Annals*[J], 2005, 54(1): 99

10 Priarone P C, Rizzuti S, Ruffa S *et al. The International Journal of Advanced Manufacturing Technology*[J], 2013, 69: 483

11 Ren Z H, Feng R C, Cao H *et al. Journal of Manufacturing Processes*[J], 2024, 119: 118

12 Ren Z H, Feng R C, Zhou B C *et al. Journal of Manufacturing Processes*[J], 2024, 132: 615

13 Klein T, Usategui L, Rashkova B *et al. Acta Materialia*[J], 2017, 128: 440

14 Fang H Z, Wang S, Chen R R *et al. Nanoscale*[J], 2021, 13(29): 12565

15 Duan B H, Yang Y C, He S Y *et al. Journal of Alloys and Compounds*[J], 2022, 909: 164811

16 Karimi P, Keshavarz M K, Sadeghi E *et al. Additive Manufacturing*[J], 2023, 77: 103811

17 Zhang Z, Zhuo J C, Niu K N *et al. Materials & Design*[J], 2024, 248: 113478

18 Xiang H G, Guo W L. *International Journal of Plasticity*[J], 2022, 150: 103197

19 Monchoux J P, Luo J S, Voisin T *et al. Materials Science and Engineering A*[J], 2017, 679: 123

20 Zhao W J, He M Q, Li C L *et al. Metals*[J], 2024, 14(7): 779

21 Zhou X, Wang S P, Lu Z T *et al. Acta Mechanica Sinica*[J], 2025, 41(2): 124030

22 Cao H, Wang J Q, Zhou B C *et al. Rare Metal Materials and Engineering*[J], 2024, 53(2): 396

23 Cao H, Xu H Z, Li H P *et al. Rare Metal Materials and Engineering*[J], 2025, 54(3): 569

24 Schuh C A. *Materials Today*[J], 2006, 9(5): 32

25 Kuksenko V, Roberts S, Tarleton E. *International Journal of Plasticity*[J], 2019, 116: 62

26 Rominiyi A L, Mashinini P M. *Ceramics International*[J], 2023, 49(2): 2194

27 Wang Y W, Raabe D, Klüber C *et al. Acta Materialia*[J], 2004, 52(8): 2229

28 Filippov P, Koch U. *Materials*[J], 2019, 12(22): 3688

29 Ernst B, Keim S, Tetzlaff U. *Materials Science and Engineering A*[J], 2022, 848: 143392.

30 Tang P, Feng J Y, Wan Z P *et al. Ceramics International*[J], 2021, 47(14): 20298

31 Li K D, Li J S, Tang B *et al. Journal of Materials Research and Technology*[J], 2021, 13: 1521

32 Wang Z F, Zhang J J, Ma A X *et al. Materials Today Communications*[J], 2020, 25: 101314

33 Viswanathan G, Lee E, Maher D M *et al. Acta Materialia*[J], 2005, 53(19): 5101

34 Britton T, Liang H, Dunne F *et al. Proceedings of the Royal Society A: Mathematical, Physical and Engineering Sciences*[J], 2010, 466(2115): 695

35 Han F B, Tang B, Yan X *et al. Metallurgical and Materials*

Transactions A[J], 2017, 48: 2051
36 Casals O, Forest S. *Computational Materials Science*[J], 2009, 45(3): 774
37 Li L, Shen L M, Proust G *et al. Materials Science and Engineering A*[J], 2013, 579: 41
38 Das S, Yu H B, Mizohata K *et al. International Journal of Plasticity*[J], 2020, 135: 102817
39 Han F B, Tang B, Kou H C *et al. Materials Science and Engineering A*[J], 2015, 625: 28
40 Petryk H, Stupkiewicz S, Kucharski S. *International Journal of Solids and Structures*[J], 2017, 112: 209
41 Wang Z F, Zhang J J, Hassan H *et al. International Journal of Mechanical Sciences*[J], 2018, 148: 531
42 Wang Z F, Liu X, Wu S L *et al. Materials Characterization*[J], 2023, 203: 113142
43 Yin B Q, Xue X Y, Tang B *et al. Materials Science and Engineering A*[J], 2022, 831: 142283
44 Zambaldi C, Raabe D. *Acta Materialia*[J], 2010, 58(9): 3516
45 Asaro R J. *Advances in Applied Mechanics*[J], 1983, 23: 1
46 Asaro R J, Needleman A. *Acta Metallurgica*[J], 1985, 33(6): 923
47 Lan Y T, Zhong X C, Quan G F *et al. Transactions of Nonferrous Metals Society of China*[J], 2015, 25(1): 249
48 Huang Y G. *A User-Material Subroutine Incorporating Single Crystal Plasticity in the ABAQUS Finite Element Program*[D]. Cambridge: Harvard University, 1991
49 Schlögl S M, Fischer F D. *Philosophical Magazine A*[J], 1997, 75(3): 621
50 Peirce D, Asaro R J, Needleman A. *Acta Metallurgica*[J], 1983, 31(12): 1951
51 Chen R R, Liu Y L, Xue X *et al. Materials Science and Engineering A*[J], 2021, 809: 140912
52 Chen L, Edwards T E J, Gioacchino F D *et al. International Journal of Plasticity*[J], 2019, 119: 344
53 Oliver W C, Pharr G M. *Journal of Materials Research*[J], 1992, 7(6): 1564
54 Pharr G M, Herbert E G, Gao Y F. *Annual Review of Materials Research*[J], 2010, 40(1): 271
55 Yang B, Vehoff H. *Acta Materialia*[J], 2007, 55(3): 849
56 Kacher J, Eftink B P, Cui B *et al. Current Opinion in Solid State and Materials Science*[J], 2014, 18(4): 227
57 Bayerschen E, McBride A T, Reddy B D *et al. Journal of Materials Science*[J], 2016, 51: 2243
58 Zhang J J, Wang Z F, Yan Y D *et al. RSC Advances*[J], 2016, 6(64): 59206

晶体取向和晶界对γ-TiAl合金纳米压痕行为的影响

牛文帅[1]，李海燕[1,2]，曾令皓[1]，曹　卉[1,2]，陈文科[1,2]，韩晨阳[1]，冯瑞成[1,2]，陈　涛[3]
(1. 兰州理工大学 机电工程学院，甘肃 兰州 730050)
(2. 兰州理工大学 有色冶金新装备教育部工程研究中心，甘肃 兰州 730050)
(3. 常州大学 机械与轨道交通学院，江苏 常州 213164)

摘　要：为了阐述γ-TiAl的变形机理，采用纳米压痕实验和晶体塑性有限元模拟研究晶体取向和晶界对γ-TiAl合金机械性能的影响。建立了晶体塑性本构模型，得到了γ-TiAl合金单晶及晶界处的载荷-位移曲线、硬度和杨氏模量。模拟数据与实验数据的误差较小，证实了纳米压痕可以很好地验证晶体塑性本构参数。基于上述模型，讨论了各晶粒和晶界压痕周围的堆积形貌，分析了不同晶体取向下累积剪切应变的分布、滑移系的启动情况、晶界与位错滑移的相互作用。结果表明，由于压头的几何形状、材料滑移系统和累积剪切应变分布之间的耦合作用，γ-TiAl合金的力学响应和堆积行为表现出显著的各向异性。此外，晶界与位错滑移的相互作用显著改变了位错的分布，进而影响了材料的流动，对材料力学响应和塑性变形起着至关重要的作用。晶界吸收了部分位错，改变了压痕下塑性变形的分布特征，导致其硬度降低，材料堆积形貌发生改变，堆积减少。

关键词：晶界；纳米压痕；各向异性；晶体取向；晶体塑性有限元

作者简介：牛文帅，男，1997年生，硕士，兰州理工大学机电工程学院，甘肃 兰州 730050，电话：0931-5135199，E-mail：191379356@qq.com